



**Effect of Extended Strain Fields on Point Defect Phonon Scattering in Thermoelectric Materials**

Journal:	<i>Physical Chemistry Chemical Physics</i>
Manuscript ID:	CP-ART-04-2015-002174.R1
Article Type:	Paper
Date Submitted by the Author:	18-Jun-2015
Complete List of Authors:	Ortiz, Brenden; Colorado School of Mines, Material Science Peng, Haowei; National Renewable Energy Laboratory, Lopez, Armando; Colorado School of Mines, Chemical Engineering Parilla, Philip; National Renewable Energy Laboratory, Lany, Stephen; National Renewable Energy Laboratory, Toberer, Eric; Colorado School of Mines, Physics

# Effect of Extended Strain Fields on Point Defect Phonon Scattering in Thermoelectric Materials †

Brenden R. Ortiz,<sup>\*a</sup> Haowei Peng,<sup>b</sup> Armando Lopez,<sup>a</sup> Philip Parilla<sup>b</sup>, Stephan Lany,<sup>b</sup> and Eric S. Toberer<sup>a</sup>

Received Xth XXXXXXXXXX 20XX, Accepted Xth XXXXXXXXXX 20XX

First published on the web Xth XXXXXXXXXX 200X

DOI: 10.1039/b000000x

The design of thermoelectric materials often involves the integration of point defects (alloying) as a route to reduce the lattice thermal conductivity. Classically, the point defect scattering strength follows from simple considerations such as mass contrast and the presence of induced strain fields (e.g. radius contrast, coordination changes). While the mass contrast can be easily calculated, the associated strain fields induced by defect chemistry are not readily predicted and are poorly understood. In this work, we use classical and first principles calculations to provide insight into the strain field component of phonon scattering from isoelectronic point defects. Our results also integrate experimental measurements on bulk samples of SnSe and associated alloys with S, Te, Ge, Sr and Ba. These efforts highlight that the strength and extent of the resulting strain field depends strongly on defect chemistry. Strain fields can have a profound impact on the local structure as in the case of Ba alloys, wherein the fields have significant spatial extent (1 nm in diameter) and produce large shifts in the atomic equilibrium positions (up to 0.5 Å). Such chemical complexity would suggest that computational assessment of point defects for thermal conductivity depression should be hindered. However, in this work, we present and verify several general descriptors that correlate well with the experimentally measured strain fields. Furthermore, these descriptors are conceptually transparent and computationally inexpensive, allowing computation to provide a pivotal role in the screening of effective alloys. The further development of point defect engineering could complement or replace nanostructuring when optimizing the thermal conductivity, offering the benefits of thermodynamic stability, and providing more clearly defined defect chemistry.

## 1 Introduction

The development of advanced thermoelectric materials would enable a broad range of technological improvements from waste heat recovery to solid-state refrigeration to novel solar-thermal energy generation.<sup>1–3</sup> Such advances depend critically on developing materials with a high thermoelectric figure of merit,  $zT$ . As such, the challenge is to predict and control the interdependent electronic and thermal properties within  $zT$ :

$$zT = \frac{S^2 \sigma T}{\kappa} \quad (1)$$

where  $T$  is the temperature,  $S$  is the Seebeck coefficient,  $\sigma$  is the electrical conductivity, and  $\kappa$  is the total thermal conductivity (electronic plus lattice contributions). Historically, searches for high  $zT$  materials have been led by experiment and heavily based on chemical intuition and simple design principles.<sup>4,5</sup> In recent years, the thermoelectric community has experienced a paradigm shift towards the high-

throughput prediction and computation of  $zT$ .<sup>6–10</sup> To date, high-throughput approaches have evaluated  $zT$  using ground-state electronic and phonon calculations. While these searches are expected to greatly accelerate the identification of promising thermoelectric materials, current approaches focus on compounds with integer stoichiometry and do not explicitly consider the potential for materials engineering.

Regardless of the search modality, achieving high  $zT$  ultimately requires extensive tailoring of microstructure and composition. Reductions in the lattice thermal conductivity  $\kappa_L$  are often achieved through nanostructuring (boundary scattering) and isoelectronic alloying (point defect scattering).<sup>11–20</sup> Point defect scattering from isoelectronic defects is a critical component of mature thermoelectric materials (e.g.  $\text{Si}_{0.8}\text{Ge}_{0.2}$ ,  $\text{PbTe}_{1-x}\text{Se}_x$ ).<sup>11–13</sup> While nanostructured materials have been extensively investigated over the last two decades,<sup>14–20</sup> point defect scattering has seen comparatively less study and has yet to be included in high throughput searches. Compared to nanostructure-based phonon scattering, point defect scattering offers the benefits of thermodynamic stability, greater applicability to anisotropic materials, and more clearly defined defect chemistry.

\* To whom correspondence should be addressed

<sup>a</sup> Colorado School of Mines

<sup>b</sup> National Renewable Energy Laboratory

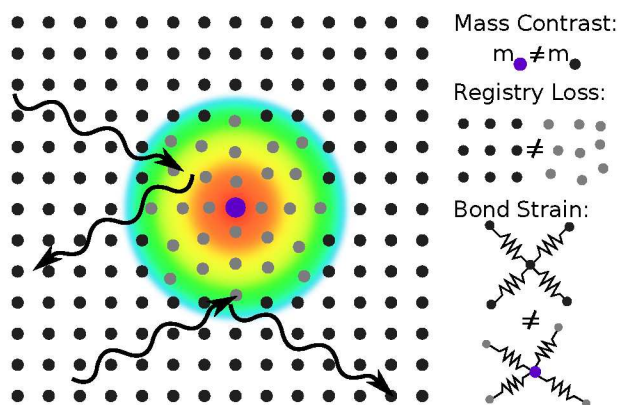


**Fig. 1** Schematic highlighting the primary factors which influence the strength of point defect scattering of phonons. The impurity atom (purple) has been substituted for a host atoms, leading to mass contrast and an extended strain field. The strain field disrupts atomic registry and strains local bonds.

Point defect scattering can be described using classical interpretations of phonon transport through a crystal lattice (Figure 1). Considering a phonon whose normal mode is supported by the host matrix, the normal mode's frequency is a reflection of the crystal symmetry, bond strengths, and mass of the constituent atoms. In the vicinity of a point defect, the same normal mode is not necessarily supported. Akin to deformation potential scattering of electrons, the strength of phonon scattering at the defect depends on the magnitude of the shift in frequency of phonon modes near the defect. The point defect scattering strength is thus determined by the structural parameters which alter the supported phonon modes: (i) mass contrast, (ii) loss of registry within the host lattice, and (iii) changes in bond strength due to bond strain (for anharmonic interactions). Additionally, the distortion may locally alter bond anharmonicity and increase the phonon-phonon Umklapp scattering rate. The impact of point defects on the phonon dispersion and associated group velocity is typically less significant. Notable exceptions are the ‘rattling’ skutterudite and clathrate compounds, wherein guest atom effects on the phonon dispersion and thermal conductivity can be profound.<sup>21–26</sup>

Point defect scattering has historically been treated using mass contrast and ‘strain field’ terms, where the strain field is a chemically ambiguous concept that depends primarily on the atomic radii contrast between the host and alloying species.<sup>27–30</sup> While mass contrast is readily calculated, accurately predicting the strain field scattering remains an outstanding challenge. In complex semiconductors, the situation is further complicated by the large number of possible alloying species and alloying sites. Experimentally, such chemical diversity leads to an overwhelming number of compositions to

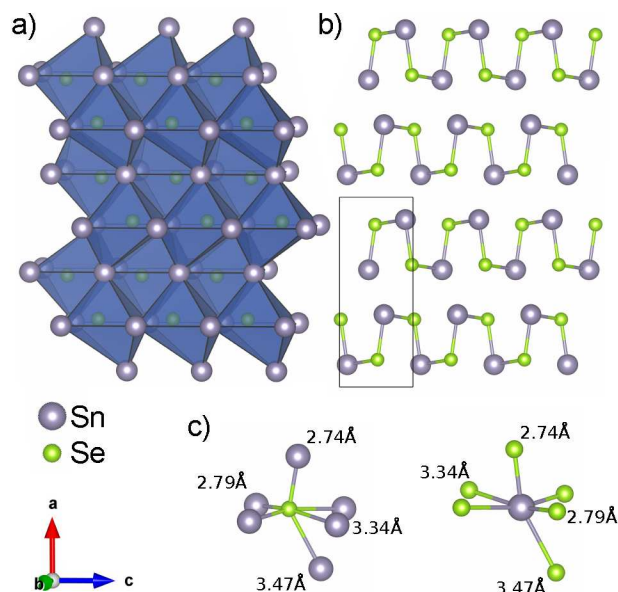


**Fig. 2** a) *Pnma* SnSe shown with polyhedra to emphasize the sheared octahedral coordination environments. b) Bonding in SnSe is heavily anisotropic, as evidenced by the accordion-like sheets of atoms formed when only considering bonds under 3Å. c) The coordination environments for Se and Sn atoms, respectively, illustrate the heavily distorted bond lengths and bond angles. The sheared octahedral coordination is what classifies SnSe as a ‘distorted rock-salt.’

consider. Computationally, the loss of short-range periodicity in the vicinity of a point-defect complicates direct prediction of the electronic and thermal properties. This is particularly unfortunate, because computational guidance could accelerate experimental optimization of thermoelectric materials by screening out ineffective alloys. To date, computational prediction of point defect scattering has only been realized in a few simple model materials (e.g. isotope scattering in GaN and  $\text{Mg}_2\text{Si}_{1-x}\text{Sn}_x$  alloys).<sup>31,32</sup> These fully ab-initio methods provide insight into the underlying transport physics but are computationally too costly for high-throughput screening. In this context, our goal is to (a) define and validate computationally inexpensive approaches to access the scattering strength of various point defect species and (b) consider the local strain field chemistry to identify material design strategies.

For our study, we seek a model system with (i) chemical diversity in the possible alloying species, (ii) sufficient structural complexity to ensure the model is robust and able to be generalized beyond high-symmetry materials, and (iii) relevance to the thermoelectric community. To this end, we have adopted SnSe as our model system. Unlike the heavier Group IV chalcogenides (e.g. PbTe), which crystallize in the rock-salt crystal structure, SnSe crystallizes as the more complex

orthorhombic *Pnma* structure (Figure 2). SnSe is often considered a layered, ‘distorted rock-salt.’ Relative to a true rock-salt structure, an apparent shear between layers results in highly distorted coordination shells. It is worth mentioning the energetic proximity ( $\sim 11$  meV) of a diffusion-less, crystallographic phase transition to the *Cmcm* phase of SnSe.<sup>33,34</sup> The *Cmcm* phase retains the orthorhombic, sheared, layered structure characteristic of *Pnma* SnSe, but the magnitude of the shear is less extreme, resulting in a more symmetric coordination environment around the Sn and Se atoms. *Pnma* SnSe is known to be fully soluble with several species (e.g. Ge, S).<sup>35,36</sup> Pure SnSe has been reported to possess high  $zT$  in the high temperature *Cmcm* phase, although there are some discrepancies in the literature.<sup>37,38</sup>

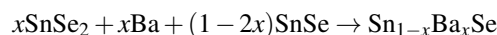
Herein, we first investigate the alloy space of SnSe through bulk synthesis to determine systems with sufficient solubility to use as a model set. We then characterize the thermal transport within the alloys, focusing on the experimental thermal conductivity. We analyze the data using classical models by Debye-Callaway and Abeles, which allow us to characterize the type of scattering observed in the system (e.g. Umklapp phonon-phonon, boundary, and point defect scattering) and determine the functional relationship between alloy composition and the thermal conductivity. Afterwards, we present three computational approaches which access the structural distortions associated with point defects and parameterize the results as simple metrics which can readily be compared against other alloying options. By combining our experimental and computational data, we show that the computational methods provide predictions which correlate well with physical observations. We find that the models successfully rank the various alloys based on their efficacy as a phonon scattering source (e.g. depression of thermal conductivity). The success of these computational models for predicting relative point defect scattering strength (a) provides a new resource for both computationally driven high-throughput searches and experimentally led synthetic surveys and (b) offers design strategies to tailor the local strain field chemistry.

## 2 Methods

### 2.1 Experimental

For isoelectronic alloying in SnSe, we focused on elements with preferred oxidation states of +2 or -2: Ca (Alfa 99.5+% granules), Sr (Alfa 99+% pieces), Ba (Alfa 99.2+% chunk), Cu (Alfa 99.9% shot), Zn (Alfa 99.99% shot), Ge (Alfa 99.9999% chunk), Te (Alfa 99.999% powder), and S (99.5+% powder). We chose to omit Pb, Cd, and Hg due to toxicity concerns. Other transition metals were omitted due to variable oxidation state and high melting points. All elements, powders, and pellets were handled in an argon glove box.

**Synthesis:** Alloys of the form  $\text{Sn}_{1-x}\text{X}_x\text{Se}$  (X: Ca, Sr, Ba, Cu, Zn, Ge) were synthesized by combination of in-house prepared SnSe, SnSe<sub>2</sub>, and the alloying species. SnSe is prepared by direct combination (melting) of Sn (Alfa 99.99% shot) and Se (Alfa 99.999% shot) at 625°C in an evacuated ( $10^{-3}$  torr) fused silica ampule. SnSe<sub>2</sub> is prepared by ball-milling SnSe with Se for 1h, followed by an anneal at 625°C. The chosen cation species have relatively high melting points; direct combination of elements in these cases can cause dangerous pressures of Se vapor to form, increasing the chance of ampule rupture. Using SnSe<sub>2</sub> as an effective selenium source entirely eliminates the chance of rupture and allows reactions to be carried out at higher temperatures. A sample reaction is:



Samples were sealed in evacuated ( $10^{-3}$  torr) fused silica ampules and heated to 1000°C at a rate of 200°C/h. Samples were soaked at 1000°C for 18h before cooling freely within the furnace. Material was agitated twice during the 1000°C soak to facilitate mixing.

Alloys of the form  $\text{SnSe}_{1-x}\text{X}_x$  (X: S, Te) were synthesized by direct combination (melting) of the raw elements. Risk of rupture is negligible due to the low melting points of S and Te. Reactants were sealed in evacuated fused silica ampules and heated to 400°C at a rate of 400°C/h. After soaking at 400°C for 12h, samples were heated to 1000°C at a rate of 100°C/h. Samples were soaked at 1000°C for 18h before cooling freely within the furnace. Samples were agitated twice during the 1000°C soak to facilitate mixing.

**Powder Characterization:** Resulting ingots were powdered using an agate mortar and pestle. Powders were passed through a 100  $\mu\text{m}$  sieve meeting ASTM E11 standards. X-ray diffraction (XRD) patterns were obtained using a Phillips X’Pert diffractometer in an  $\theta$ - $2\theta$  configuration using a Cu K $\alpha$  radiation source. Patterns were refined using the Rietveld method within the General Structure Analysis System (GSAS) as distributed by Argonne National Laboratory.<sup>39,40</sup> Except where noted, refinements use the *Pnma* SnSe crystal (ICSD: 041740) as the base structure. In anticipation of applying Vegard’s Law, we refine primarily on the lattice parameter, typical peak broadening terms, and preferential orientation. To ensure uniformity in texturing, additional diffraction data was collected using a Bruker D8 diffractometer and an area detector.

**Pellet Compaction:** Samples were inductively pressed in high-density graphite dies (POCO) under 100 MPa of pressure. Hot pressing was conducted under 7-8 torr of argon to counter the innately high vapor pressure of SnSe. Samples were pressed at 525°C for 45m. Resulting pellets are cylindrical, approximately 13mm in diameter and 10mm in height.

**Pellet Characterization:** Prior work on hot pressed SnSe has demonstrated a high degree of texturing parallel to the direction of applied pressure.<sup>38</sup> This is consistent with the layered structure of SnSe. In accordance with prior work,<sup>38</sup> sintered pellets of SnSe were sectioned into two plates using a Buehler IsoMet low speed saw: a plate with the primary surface perpendicular to the press axis, and a plate with primary surface parallel to the press axis. XRD was performed on all sectioned plates to determine the degree of texturing, and confirm phase purity. Sectioned pellets were polished with a series of sandpapers, terminating at 2000 grit. Polished samples were coated in Graphit graphite spray. Thermal diffusivity was measured using a Netzsch Laser Flash Apparatus (LFA) 457. Diffusivity data is fit using a Cowen plus Pulse Correction (CPC) numerical model. The total thermal conductivity of the alloyed samples was calculated using:

$$\kappa = D\rho C_p \quad (2)$$

where  $D$  is the thermal diffusivity,  $\rho$  is the mass density, and  $C_p$  is the heat capacity. The heat capacity is estimated using the Dulong-Petit approximation.

Despite experimental densities commonly exceeding 97% of the theoretical density, all samples include a correction for porosity using two-component, three-dimensional Bruggeman model for a composite with spherical inclusions,<sup>41,42</sup>

$$\sum_i \delta_i \frac{\kappa_i - \kappa_e}{\kappa_i + 2\kappa_e} = 0 \quad (3)$$

where  $\delta_i$  is the volume fraction of component  $i$ ,  $\kappa_i$  is the conductivity of component  $i$ , and  $\kappa_e$  is the effective (measured) conductivity of the sample. Allowing the sum over two components, the porosity and sample conductivity,  $\kappa_i = (\kappa_{\text{Void}}, \kappa_{\text{SnSe}})$ , and solving for  $\kappa_{\text{SnSe}}$  gives the porosity-corrected thermal conductivity. We approximate  $\kappa_{\text{Void}}$  as that of argon gas (the gas present during pressing), which is effectively zero compared to the conductivity through the solid media.

Speed of sound measurements were performed using an Olympus 5072PR Pulser/Receiver system with a gain of 30 dB and a 5 kHz signal. Both transverse and longitudinal measurements were made, using Olympus V112 (longitudinal) and Olympus V156 (transverse) transducers. Data was collected and analyzed on an Atten ADS 1102C oscilloscope.

Room temperature Hall effect measurements were made using a BioRad HL5500 PC with a probe current between 1-10 mA. Results indicate that the carrier concentration remains p-type, roughly  $10^{17} \text{cm}^{-3}$  regardless of composition. Due to the low intrinsic carrier concentration of SnSe, the electronic contribution to the thermal conductivity is negligible and  $\kappa \approx \kappa_L$ .

## 2.2 Computational

**Nuclear PDF Calculations:** We used a 32-atom special quasi-random structure (SQS)<sup>43</sup>, generated with the ATAT package<sup>44</sup>, to model both the cation and anion-site alloys. For alloys containing 25% cation or anion substitution, the SQS can only mimic the pair correlation function up to the 4th nearest neighbor. To compensate, we perform 4 unique calculations and average over the respective quantities of interest. The atomic structure of the SQSs were relaxed using the VASP code<sup>45</sup> within the local density approximation (LDA)<sup>46</sup>. The ion-electron interactions were described with the projector augmented wave (PAW) method<sup>45,47</sup>. Lattice vectors and atomic coordinates of the alloys were allowed to relax to minimize the stress tensor and interatomic forces. We minimize the diagonal elements of the stress tensor such that the underlying primitive lattice is always orthorhombic. We then compute the nuclear pair distribution function  $g(r)$ , given by

$$g(r) = \frac{dn(r)}{4\pi\rho_0 r^2 dr} \quad (4)$$

where  $dn(r)$  is the number of atoms in the shell between  $r + dr$  with respect to the reference atom, and  $\rho_0$  is the number density of atoms.

**Single Atom Model:** The density functional calculations were performed in the generalized gradient approximation (GGA)<sup>48</sup> using the VASP code<sup>45</sup>. For the structural relaxation of the S, Te, Ge, Sr, and Ba impurities, we used a 2x4x4 supercell containing 256 atoms and included the relaxations of atoms up to a cutoff radius of 8 Å around the lattice site where the impurity was substituted. For these supercell calculations, we used an energy cutoff of 330 eV and a 2x2x2 k-mesh for Brillouin zone sampling.

**Bulk Modulus:** The bulk modulus was obtained by calculating the total energy  $E$  in LDA as a function of cell volume  $\Omega$ , and fitting the bulk modulus  $B_0$  and its associated pressure derivative  $B_0'$  to the Murnaghan equation of state:<sup>49</sup>

$$E(\Omega) = E_0 + \frac{B_0\Omega}{B_0'} \left( \frac{(\Omega_0/\Omega)^{B_0'} + 1}{B_0' - 1} \right) - \frac{B_0\Omega_0}{B_0' - 1}. \quad (5)$$

here  $E_0$  and  $\Omega_0$  are the equilibrium total energy and volume,  $B_0$  and  $B_0'$  are the bulk modulus at zero pressure, and the pressure derivative of the bulk modulus.

## 3 Results and Discussion

### 3.1 Experimental Results

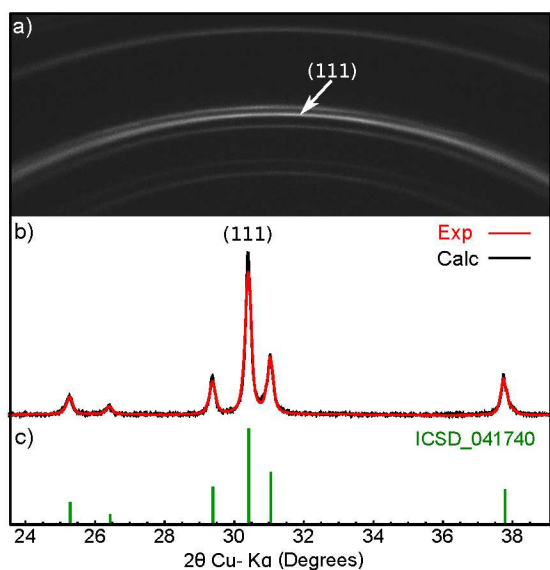


**Fig. 3** a) High-quality polycrystalline material confirmed by continuity of Debye rings in Debye-Scherrer diffraction pattern of SnSe. b) Independently collected Bragg-Brentano diffraction data demonstrates that synthesized material is phase pure, as seen by excellent agreement between experimental (black) and calculated (red) data. Only a small section of  $2\theta$  is shown to highlight relative intensities and correspondence with Debye rings. See Figure S1 for full range. c) Samples match relative intensity profile (green) of randomly oriented SnSe.

**Structure:** Prior experimental efforts have found SnSe to be challenging to form as isotropic, dense ingots.<sup>38</sup> The optimized synthetic approach developed here, in which inductive hot pressing follows melt synthesis, yields single phase pellets with densities  $>97\%$  of the theoretical density obtained from XRD refinement. The only notable low density samples are those containing  $>5$  mol% Ba, where densities were  $>90\%$ . We have determined that sections of sample taken from the interior of the pellet, cut parallel to the press axis, demonstrate XRD patterns consistent with randomly-oriented polycrystalline SnSe.

Figure 3a demonstrates a section of a Debye-Scherrer 2D diffraction pattern. Continuity of the Debye rings is consistent with expected behavior for samples with randomly oriented crystallites. All rings in the Debye-Scherrer pattern can be indexed to a corresponding peak in the Bragg-Brentano  $\theta$ - $2\theta$  scan shown in Figure 3b. The (111) peak is the strongest reflection for randomly oriented powder. Note that  $\theta$ - $2\theta$  data was obtained and refined from 12 to 80 degrees of  $2\theta$ . We show only a small region of the XRD scan in order to highlight the correspondence between the Debye-Scherrer and Bragg-Brentano approaches. Rietveld refinement confirms that material is phase pure within the resolution of XRD.

**Table 1** Results obtained from the preliminary solubility study.

Experimental results are shown adjacent to literature values, where applicable. Where phase separation is observed, resulting secondary phases are given.

Alloy	Exp. (mol%)	Lit. (mol%)	Phases	Ref
Ge	$>32$	Full	None	35
S	$>32$	Full	None	36
Te	16-32	20	SnSe + SnTe	50
Ba	16-32	–	SnSe + BaSe	–
Sr	5-7	–	SnSe + SrSe	–
Ca	1-2	–	SnSe + CaSe	–
Zn	$<1$	$<1$	SnSe + ZnSe	51
Cu	$<1$	–	SnSe + Cu <sub>2</sub> SnSe <sub>3</sub>	–

Slices of sample taken from the edges of the pellet, perpendicular to the press axis, demonstrate significant texturing along the (040) set of crystallographic planes, consistent with the layered crystallography of SnSe (Figure S1). Due to the anisotropic transport expected of SnSe, we omit analysis of these exterior slices and focus on the properties of the randomly-oriented SnSe sections, wherein the relationship between the transport and crystallography is more easily described.

**Alloying and Solubility:** To isolate the effect of point defect scattering on the thermal conductivity, it is essential to establish solubility limits for each element. Phase separation can lead to the evolution of complex microstructures or nanoprecipitates; both of which are known to have a *profound* effect on the thermal conductivity.<sup>14–20</sup>

To serve as a coarse down-selection, an initial solubility study was performed over a wide array of alloying species: Ca, Sr, Ba, Cu, Zn, Ge, S, and Te via bulk synthesis (Table 1). Note that the composition steps taken were not linear, and were focused on dilute alloys ( $<10$  mol%). As such, solubility determinations  $>10$  mol% are very coarse. We did not exceed 32 mol% in our study. Solubility determinations were made based on two primary observations: shifts in the lattice parameters, and the evolution of secondary phases. Our experimental values agree with existing phase diagrams for Ge, S, Te, and Zn.<sup>35,36,50,51</sup> However, literature does not exist for alloys containing Cu, Ca, Ba, and Sr in bulk SnSe. We have demonstrated significant solubility of Sr and Ba in SnSe under ambient conditions. Conversely, we have also demonstrated the low solubility of Ca and Cu.

Henceforth, experimental data will focus primarily on elements with extended solubility in SnSe ( $>2$  mol%). The 2 mol% cutoff ensures that a large enough range of sample compositions could be synthesized before phase separation. Pellets of SnSe alloys containing Sr, Ba, Ge, S, and Te were synthesized in steps of 2 mol% from 1-9 mol%. XRD was performed after hot pressing to ensure that phase purity persists

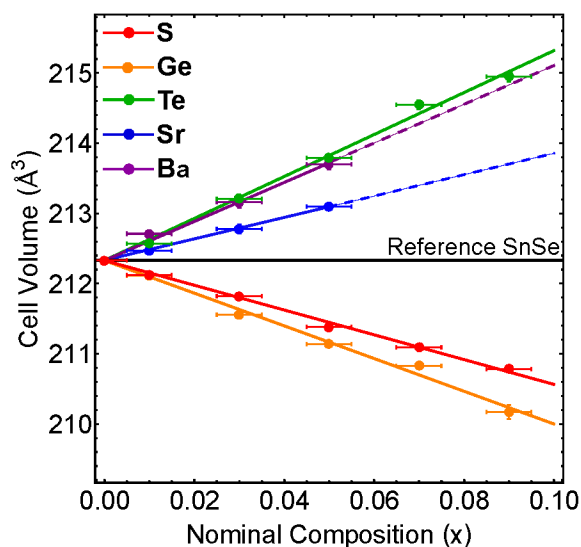


**Fig. 4** Cell volume varies linearly with alloy composition in species with solubility exceeding 2 mol%, consistent with Vegard's Law. The cell volume of pure, unalloyed SnSe (black) is shown for easy comparison. Dashed lines for Sr indicate solubility limit while dashed lines for Ba indicate changes in crystallography which inhibit clear comparison with other alloy systems. Error bars for the cell volume represent  $3\sigma$  from the mean, but are too small to be resolved on the plot.

after pressing and annealing. All XRD scans are provided in Figure ???. Plots demonstrating trends in the cell volume and  $b/c$  lattice parameter ratio are shown in Figures 4 and 5, respectively.

The shifts in cell volume shown in Figure 4 demonstrate a linear dependence on the alloying composition, consistent with the classical interpretation of Vegard's Law. A notable expansion of the unit cell is seen with the addition of Sr or Ba. It is not clear whether one can use the difference in atomic radii to justify the volumetric expansion seen in Sr and Ba alloys. The inherently mixed bonding character of Sr and Ba in SnSe makes the choice of atomic radii (ionic or covalent) unreliable. However, the average atomic volume assigned to the cation site in rock-salt SrSe ( $\sim 30.6 \text{ \AA}^3$ ) is larger than the cation site in SnSe ( $\sim 26.5 \text{ \AA}^3$ ). Integration of Sr into SnSe likely results in a change in the local coordination towards that of SrSe, consistent with the observed volumetric expansion. The analogy can be extended to Ba as well. This is particularly interesting, as it suggests that the local environment surrounding the Sr and Ba atoms is shifting to accommodate the preferred bonding of the alloying species.

Examination of the ratio of  $b$  and  $c$  lattice parameters reveals further evidence suggesting that the SnSe structure is highly tolerant of non-isostructural defects. Literature reveals that the phase transition in SnSe from the  $Pnma$  to  $Cmcm$

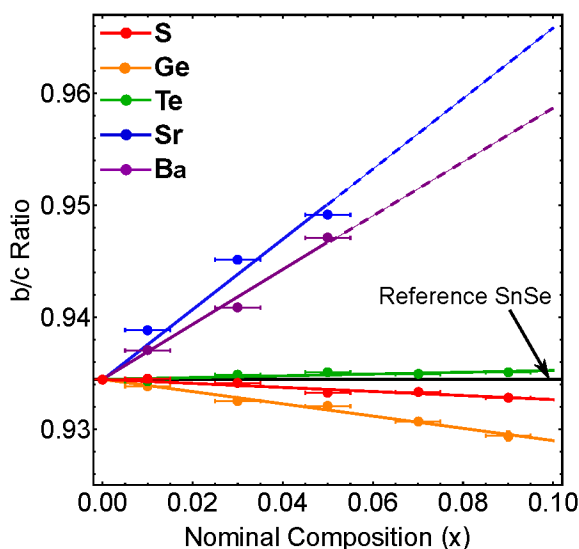


**Fig. 5** The crystallographic phase change in SnSe from the  $Pnma$  to  $Cmcm$  phase is marked by a change in the  $b/c$  lattice parameter ratio from  $b/c < 1$  to  $b/c > 1$ .<sup>33</sup> Alloys of Sr and Ba demonstrate behavior consistent with a gradual transition towards the  $Cmcm$  structure. This suggests significant distortion of the crystal lattice surrounding Ba and Sr point defects. The  $b/c$  ratio for pure, unalloyed SnSe (black) is shown for easy comparison. Error bars for the  $b/c$  ratio represent  $3\sigma$  from the mean value, but are too small to be resolved on the plot.

phase is marked by a reversal in the  $b/c$  ratio from  $b/c < 1$  to  $b/c > 1$  at elevated temperatures.<sup>33</sup> Figure 5 demonstrates the experimentally observed shift in the  $b/c$  ratio for SnSe as a function of alloying species and composition. We observe strong increases in the  $b/c$  ratio with the addition of Sr and Ba. This can be understood by considering the local bonding of SnSe in the  $Pnma$  and  $Cmcm$  phases and the preferred bonding of Sr and Ba in SrSe and BaSe. The  $Cmcm$  phase is marked by distinctively less shear between individual layers, which reduces the degree of distortion seen in individual polyhedra. Incorporation of elements where the selenide end-member (SrSe, BaSe) is a true rock-salt with octahedral coordination, could be expected to distort the structure towards the  $Cmcm$  phase, which is consistent with the behavior observed for Sr and Ba alloys.

**Barium Alloys:** At first glance, the behavior of the Ba alloys is similar to Sr in SnSe. However, alloys containing more than 5 mol% Ba begin to diverge significantly from the formalism provided by Vegard's Law. When refining alloys containing Ba, the parent  $Pnma$  SnSe structure is only valid up to 5 mol%. Above 5 mol% Ba, additional peaks begin to appear in the XRD pattern. Extra peaks would normally be attributed to phase separation; however, the additional peaks do not match any known phases within the Ba-Sn-Se system

or any known polymorphs of SnSe. Furthermore, peaks indexed to the parent *Pnma* structure continue to shift with addition of more Ba, as would be expected from Vegard's Law. The observed deformation is also consistent with the decrease in density for pellets containing >5 mol% Ba. Work is ongoing to characterize the exact nature of the crystallographic changes observed in SnSe alloys containing Ba. For the analysis herein, only samples up to 5 mol% Ba are considered.

**Temperature Dependent  $\kappa$ :** The thermal conductivity of SnSe and corresponding alloys are found to decay above room temperature (Figure 6). Measurements are performed on samples cut parallel to the pressing axis, for which transport is expected to be consistent with randomly oriented polycrystalline SnSe. We focus primarily on 5 mol% alloys for the temperature dependent thermal conductivity. Similar results are expected for other compositions. We observe strong decreases in the room temperature thermal conductivity with the addition of Ba or Sr (~50% reduction), and modest decreases with other alloying agents.

To examine the relative influences of point defect, Umklapp, and boundary scattering of phonons, we first examine the temperature dependent Debye-Callaway model:<sup>52,53</sup>

$$\kappa_L(T) = \int_0^{\omega_{\max}} C_s(\omega, T) v_g(\omega)^2 \tau(\omega, T) d\omega \quad (6)$$

where  $C_s(\omega, T)$  is the *spectral* heat capacity. Within the acoustic Debye approximation, the phonon group velocity within the acoustic branches  $v_g(\omega)$  can be approximated as the speed of sound  $v_s$ . This sets an upper bound on the acoustic frequency given by:

$$\omega_{\text{Acoustic}} = \frac{k\Theta}{n^{1/3}\hbar} \quad (7)$$

where  $k$  is Boltzmann's Constant,  $\Theta$  is the Debye temperature,  $n$  is the number of atoms per primitive cell, and  $\hbar$  is the reduced Planck's constant.

The longitudinal and transverse speed of sound were measured for all samples, but differences in the speed of sound as a function of alloying composition and alloying species could not be resolved beyond experimental error. As such, we take the speed of sound to be composition independent at 1560 m/s, the value obtained from measurements made on pure SnSe. For additional results, refer to Table S1.

The low velocity optical branches can be treated using the minimal model for thermal conductivity,<sup>5</sup> where  $\tau = \pi/\omega$  and  $v_g(\omega)$  is approximated as  $v_s$ . Within this model, these modes extend from  $\omega = \omega_{\text{Acoustic}}$  to  $\omega = k\Theta/\hbar$ . We find that the minimum optical contribution at high temperature is approximately  $0.2 \text{ W m}^{-1} \text{ K}^{-1}$ .

The phonon scattering lifetime  $\tau$  in Equation 6 is the reciprocal sum of the individual contributions:

$$\tau^{-1} = \sum \tau_i^{-1} = \tau_U^{-1} + \tau_B^{-1} + \tau_{\text{PD}}^{-1} \quad (8)$$

Here, we consider Umklapp scattering  $\tau_U$ , boundary scattering  $\tau_B$ , and point defect scattering  $\tau_{\text{PD}}$ . The Umklapp scattering term is given as<sup>5,54</sup>

$$\tau_U = \frac{(6\pi^2)^{1/2}}{2} \frac{Mv_s^3}{k_b V^{1/3} \gamma^2 \omega^2 T} \quad (9)$$

and depends on the compound's average atomic mass  $M$ , volume per atom  $V$  and Grüneisen parameter  $\gamma$ . Boundary scattering of phonons,  $\tau_B$  is given by<sup>5,55,56</sup>

$$\tau_B = \frac{l}{v_s} \quad (10)$$

where  $l$  is related to the microstructure. The contribution to phonon scattering by point defects,  $\tau_{\text{PD}}$  is given by<sup>5,57,58</sup>

$$\tau_{\text{PD}} = \xi \frac{4\pi v_s^3}{V\omega^4} \quad (11)$$

where  $\xi$  is a defect-specific constant and is related to the mass and radii contrast between the host and alloying atom.

Within the Debye-Callaway model, the free parameters are  $\gamma$ ,  $l$ , and  $\xi$  in Equations 9, 10, and 11, respectively. To reveal the individual contributions to the phonon transport, we begin by refining  $\gamma$  and  $l$  for pure SnSe. Here the impact of point defect scattering is expected to be vanishingly small compared to alloyed samples, allowing the assumption  $\xi \approx 0$ . Initial attempts to fit data for pure SnSe yielded curves which exhibited too little dependence on  $T$  compared to the experimental data. To reconcile this, the Umklapp scattering strength was increased from  $\tau_U \propto T^{-1}$  to  $\tau_U \propto T^{-1.3}$ . The increased temperature dependence may be due to a softening of the lattice or increased anharmonicity as the *Pnma* to *Cmcm* phase transition is approached.

We expect the largest change between pure SnSe and the alloyed systems stems from the point defect scattering contained within  $\tau_{\text{PD}}$ . The boundary scattering parameter  $l$  depends largely on process parameters, which were not varied between samples. Additionally, due to the extremely strong Umklapp scattering in SnSe (Figure S3), changes in the boundary scattering parameter have extremely small effects on the overall model quality. We do not expect  $\gamma$  to vary significantly in the dilute regime (5 mol%). As such, we fix  $l$  and  $\gamma$  to the values refined from pure SnSe, taking them as composition independent parameters. Samples containing 5 mol% of each element (Sr, Ba, Ge, S, and Te) were then fit with the point defect scattering term  $\tau_{\text{PD}}$  included ( $\xi \neq 0$ ).

Resulting curves show excellent agreement with experiment (Figure 6). The success of the Debye-Callaway model in describing the thermal conductivity of SnSe and the associated alloys reveals that phonon scattering physics is well described by Equation 8.

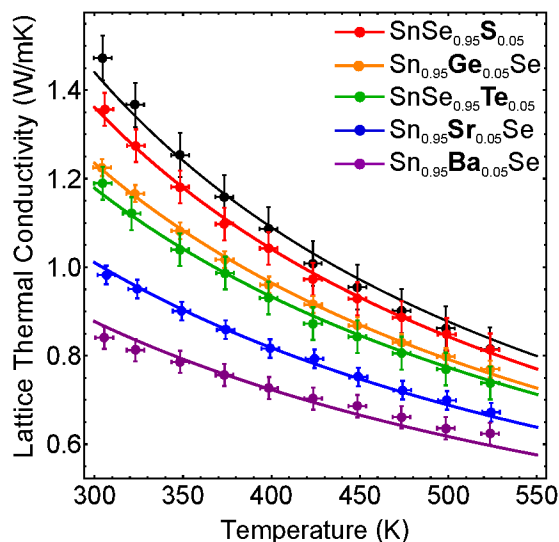


**Fig. 6** The Debye-Callaway model generates excellent fits for the temperature dependent thermal conductivity for 5 mol% alloys of SnSe. This suggests that the scattering physics is well captured by a combination of Umklapp, boundary, and point defect scattering. Error bars for the temperature and thermal conductivity correspond to  $3\sigma$  from the mean value.

### Composition Dependent $\kappa$ :

To examine the change in point defect scattering apart from Umklapp and boundary scattering, we now examine the thermal conductivity as a function of alloying composition and alloying species at fixed temperature (Figure 7).

We begin by adopting the classical interpretation of composition dependent thermal conductivity presented by Abeles.<sup>30</sup> In this interpretation, we assume that the primary sources of scattering can be broken into two terms: mass-contrast scattering and strain-field scattering. This approach has had success in describing the relationship between thermal conductivity and composition in many systems (e.g skutterudites and half-Heuslers).<sup>59–61</sup>

To estimate the thermal conductivity using this approach, we begin by defining the disorder scaling parameter,  $u$ :

$$u = \left( \frac{\pi^2 \Theta \Omega}{h v_s^2} \kappa_0 \Gamma_{\text{tot}} \right)^{1/2} \quad (12)$$

where  $\Theta$ ,  $\Omega$ ,  $h$ , and  $v_s$  stand for the Debye temperature, average atomic volume, Planck constant, and the speed of sound.  $\kappa_0$  is the lattice thermal conductivity of the pure, unalloyed material.  $\Gamma_{\text{tot}}$  is the net scattering factor, which introduces the effect of alloying as two independent scattering terms

$$\Gamma_{\text{tot}} = \Gamma_m + \Gamma_s \quad (13)$$

where  $\Gamma_m$  is the mass scattering parameter and  $\Gamma_s$  is the strain-field scattering parameter. The alloy thermal conductivity is

then set by the magnitude of  $u$ :

$$\kappa_{\text{alloy}} = \kappa_0 \left( \frac{\tan^{-1}(u)}{u} \right) \quad (14)$$

For a binary host system, with only one alloying site (e.g. cation substitution in  $\text{Sn}_{1-x}\text{Ba}_x\text{Se}$ ), the mass scattering factor is given by:

$$\Gamma_m = x(1-x) \frac{a}{a+b} \left( \frac{M_{\text{Sn},X}}{M} \right)^2 \left( \frac{\Delta M_{\text{Sn},X}}{M_{\text{Sn},X}} \right)^2 \quad (15)$$

where  $\Delta M_{\text{Sn},X}$  is the difference in atomic mass on the Sn sites.  $M$  is the apparent average atomic mass of the alloyed compound.  $M_{\text{Sn},X}$  is the average atomic mass on the Sn sites. The parameters  $a$  and  $b$  correspond to the stoichiometry of the host compound. In this case,  $\text{Sn}_1\text{Se}_1$  yields  $a = b = 1$ . The strain-field scattering parameter is given by:

$$\Gamma_s = x(1-x) \varepsilon \frac{a}{a+b} \left( \frac{M_{\text{Sn},X}}{M} \right)^2 \left( \frac{\Delta r_{\text{Sn},X}}{r_{\text{Sn},X}} \right)^2 \quad (16)$$

Here,  $\varepsilon$  is a phenomenological constraint to be fit from experiment and normally ranges from 10 to 100.<sup>30,60,61</sup>  $\Delta r_{\text{Sn},X}$  is the difference in radii on the tin sites.  $r_{\text{Sn},X}$  is the average radii of the atoms on the tin sites. When comparing the magnitude of the strain scattering for different chemistries,  $\varepsilon$  has often been used as the relevant metric. However, one of the primary ambiguities when using the Abeles Model is the choice of atomic radii in Equation 16. For some compounds (e.g.  $\text{Sn}_{1-x}\text{Ge}_x\text{Se}$ ), the bonding is largely covalent and using the covalent radii is a logically consistent decision. However, when considering alloys of Sr and Ba, the choice of atomic radii is no longer obvious. Realistically, the bonding is likely a strong mixture of both covalent and ionic bonding characters. Unfortunately, as the atomic radii will change significantly between the ionic and covalent situations, the value of  $\varepsilon$  will also change significantly. In this sense,  $\varepsilon$  in itself is not a useful construct numerically. Furthermore, the use of radii in complex semiconductors with anisotropic bonding may not capture the underlying chemistry of the distortions present.

Despite these issues with atomic radii and  $\varepsilon$ ,  $\Gamma_s$  remains a useful parameter when fit using experimental data. Ambiguity in the atomic radii is largely absorbed into  $\varepsilon$ . For the fits reported in Table 3, we choose to use the covalent radii for Sn, Se, Ge, Te, and S and the ionic radii for Sr and Ba. However,  $\Gamma_s$  in this conventional form retains a dependence on the mass contrast. For the purpose of comparing experimental fits to our computational models, it is thus desirable to develop a term that is strictly dependent on strain. To this end, factoring out  $(M_{\text{Sn},X}/M)^2$  from Equation 16 provides the reduced expression shown in Eq. 17.

$$\Gamma'_s = x(1-x) \varepsilon \frac{a}{a+b} \left( \frac{\Delta r_{\text{Sn},X}}{r_{\text{Sn},X}} \right)^2 \quad (17)$$

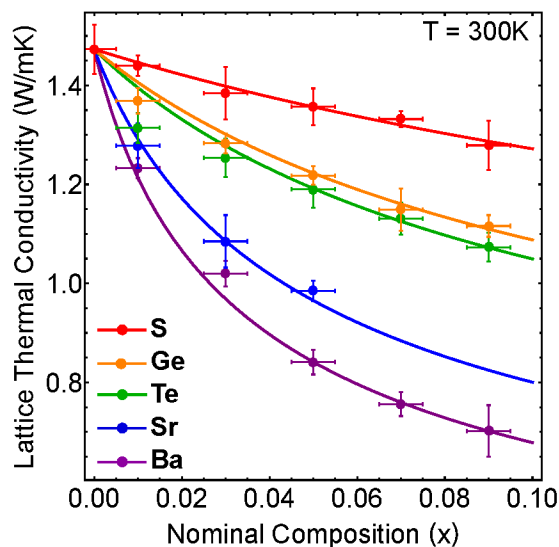


**Fig. 7** The Abeles model generates fits which agree well with the composition dependent thermal conductivity for SnSe and associated alloys of Ba, Sr, Ge, Te, and S. Strong depression of thermal conductivity observed in samples containing Sr or Ba, moderate depression observed for all other alloys. Altering the choice of atomic radii does not change the quality of the fits, only the magnitude of the free parameter  $\epsilon$ . Error bars for the composition and thermal conductivity represent  $3\sigma$  from the mean value.

Figure 7 presents the experimentally determined thermal conductivity as a function of composition. Curves are theoretical predictions obtained from the Abeles model using only  $\epsilon$  as the only free parameter. It is important to note that changes in the atomic radii *do not affect* the quality of the fit, only the relative magnitude of  $\epsilon$ . The functional form of the Abeles model fits extremely well, considering the relative simplicity of the model and the underlying assumptions. Parameters of interest, including  $\Gamma'_s$ , are provided in Table 2 for 5 mol% alloys of S, Ge, Te, Sr, and Ba. Parameters for all other compositions can be found in supplementary Table S2.

The success of the Abeles model in describing the thermal conductivity of SnSe as a function of composition (Fig. 7) reveals that the data can be functionally well understood as a combination of mass and strain-field scattering. Additionally, use of  $\Gamma'_s$  strips out contributions from mass scattering, providing us with a convenient way of quantifying the experimental strain scattering.

### 3.2 Computational Results

Characterization of the model system found 5 elements (S, Ge, Te, Sr, and Ba) with solubilities significant enough to be considered for computational assessment. For this model sys-

**Table 2** Parameters of interest for 5 mol% alloys. Shown are  $\epsilon$ ,  $\Gamma_m$ , and  $\Gamma_s$  from the classical Abeles approach, the ratio of strain to mass scattering, and  $\Gamma'_s$ . Note that  $\epsilon$  is composition *independent*, although all other parameters are explicitly dependent on composition. Due to a strong dependence on the choice of atomic radii,  $\epsilon$  is not a numerically robust quantity; it is shown for transparency only.

Alloy	$\epsilon$	$\Gamma_m$	$\Gamma_s$	$\Gamma_{\text{tot}}$	$\Gamma_s/\Gamma_m$	$\Gamma'_s$
S	0	0.0055	0	0.0055	0	0
Ge	14	0.0053	0.0089	0.0142	1.73	0.0063
Te	32	0.0056	0.0112	0.0168	1.99	0.0168
Sr	490	0.0024	0.0423	0.0447	17.8	0.0297
Ba	402	0.0008	0.0712	0.0720	85.0	0.0491

tem, three different computational routes were applied to estimate the relative point defect scattering strength: (i) the single atom distortion (SAD), (ii) bulk modulus and the pressure derivative of the bulk modulus, and (iii) the pair distribution function (PDF).

**Single Atom Distortion:** The Single Atom Distortion (SAD) approach investigates the effect of a single alloying atom on the surrounding lattice. We placed an isolated substitutional defect (e.g. one Ba atom) in a 256 atom supercell of SnSe and allowed the structure to relax within an 8 Å radius of the defect. This representation allows us to probe the effective ‘radius of influence’ of the defect and the associated effects on the local structure. Results are represented as vector plots in Figure 8. Vector direction is indicative of the displacement direction, vector color is indicative of the magnitude of the displacement. The strong distortion field associated with Sr and Ba alloys is immediately evident in Figure 8.

We seek a quantitative measure of the distortion induced by the alloying atom. To this end, we construct a sum over all atomic displacements:

$$\Delta_{\text{SAD}} = \sum_{i=1}^N |\vec{r}_{\text{Alloy},i} - \vec{r}_{\text{SnSe},i}| \quad (18)$$

where  $N$  is the number of atoms in the supercell and  $\vec{r}_{\text{Alloy},i}$  and  $\vec{r}_{\text{SnSe},i}$  are the final and initial positions of atom  $i$ , respectively. The sum is only performed if the net displacement of the atom exceeds the computational error in the relaxation. This error is estimated in the Supplementary section (Figure S4) to be  $\sim 0.04\text{\AA}$ . In Figure 8, the blue and purple atoms are not included in the calculation of  $\Delta_{\text{SAD}}$  as their displacements are less than the thermal cutoff of  $0.04\text{\AA}$ . Thus,  $\Delta_{\text{SAD}}$  provides a single scalar which can be used to compare the net distortion induced by different alloying species (Table 3). The SAD approach directly examines loss of atomic registry and implicitly carries information regarding bond strain. The vector plots also emphasize that ‘point’ defects often induce extended distortions within the host crystal (e.g. Ba and Sr have distortions

beyond 8 Å away from the initial defect site).

**Bulk Modulus:** The bulk modulus  $B_0$  and the first derivative of the bulk modulus with respect to pressure  $B'_0$  comprise our second metric (Table 3). Computations are performed on 25 mol% SQS supercells of alloyed SnSe. While we do not examine samples with 25 mol% experimentally, the computation of  $B_0$  or  $B'_0$  is inherently a representation of the *average* bond strength; results should be analogous at lower concentrations as well. Changes in  $B_0$  represent a change in the distribution of bond strengths surrounding the associated point defect, which alters the locally supported phonon modes. Analogous to the loss of atomic registry,  $B_0$  lets us probe the loss of ‘bond strength registry.’ With the addition of  $B'_0$ , we can

also probe the change in anharmonicity, related to the material’s deviation from parabolic (harmonic) behavior.  $B'_0$  is indirectly related to the Grüneisen parameter, another measure of the material’s anharmonicity.<sup>62</sup> Results of the calculations are provided in Table 3. We generally see a softening of the lattice with the addition of point defects, particularly so with the addition of Sr or Ba (~25% decrease with Ba).

**Pair Distribution Function:** Our final metric is the pair distribution function (PDF), a direct-space representation of the coordination environment of a given structure. The PDF can be thought of as a ‘fingerprint’ of the coordination environment of the reference structure. By comparing the PDF pattern for pure SnSe with the alloys, we can investigate the

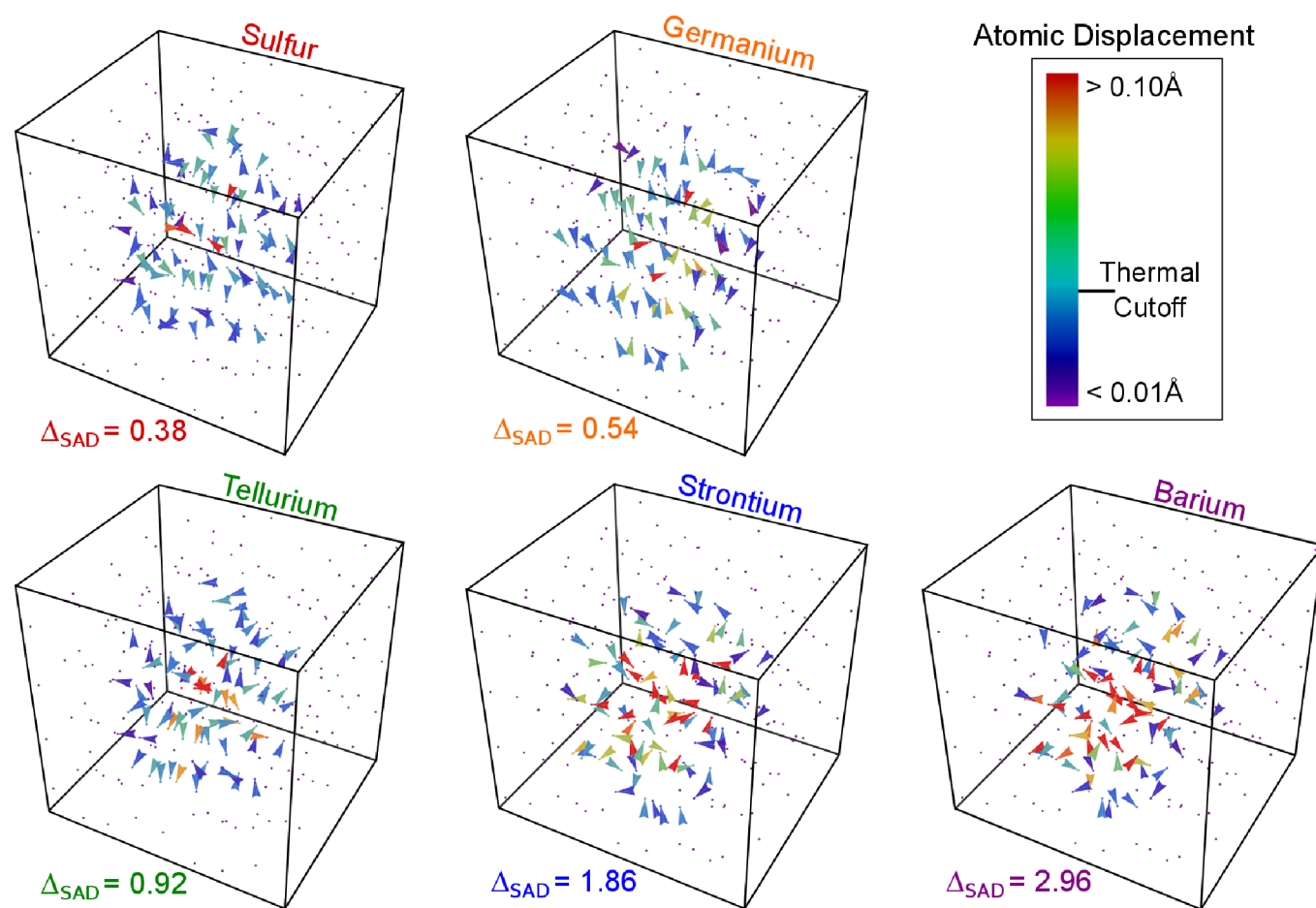


**Fig. 8** Vector plots and associated distortion metric  $\Delta_{\text{SAD}}$  provide an alternative representation of the distortion induced by a given point defect in terms of atomic motion surrounding an individual defect site. Vector direction is representative of the direction of atomic displacement, while vector color is related linearly to the magnitude of the displacement. We see strong (red and orange) displacements surrounding the Sr and Ba point defects and extending several coordination shells outward. Conversely, the distortion in Te, Ge, and S is relatively smaller and more localized in the immediate vicinity of the defect. All alloys highlight that ‘point’ defects can cause extended distortions away from the defect site which may significantly alter the local crystallography and the supported phonon modes. Displacements below the thermal cutoff are not included in calculation of  $\Delta_{\text{SAD}}$  (See Figure S4 for details on the determination of the thermal cutoff value).

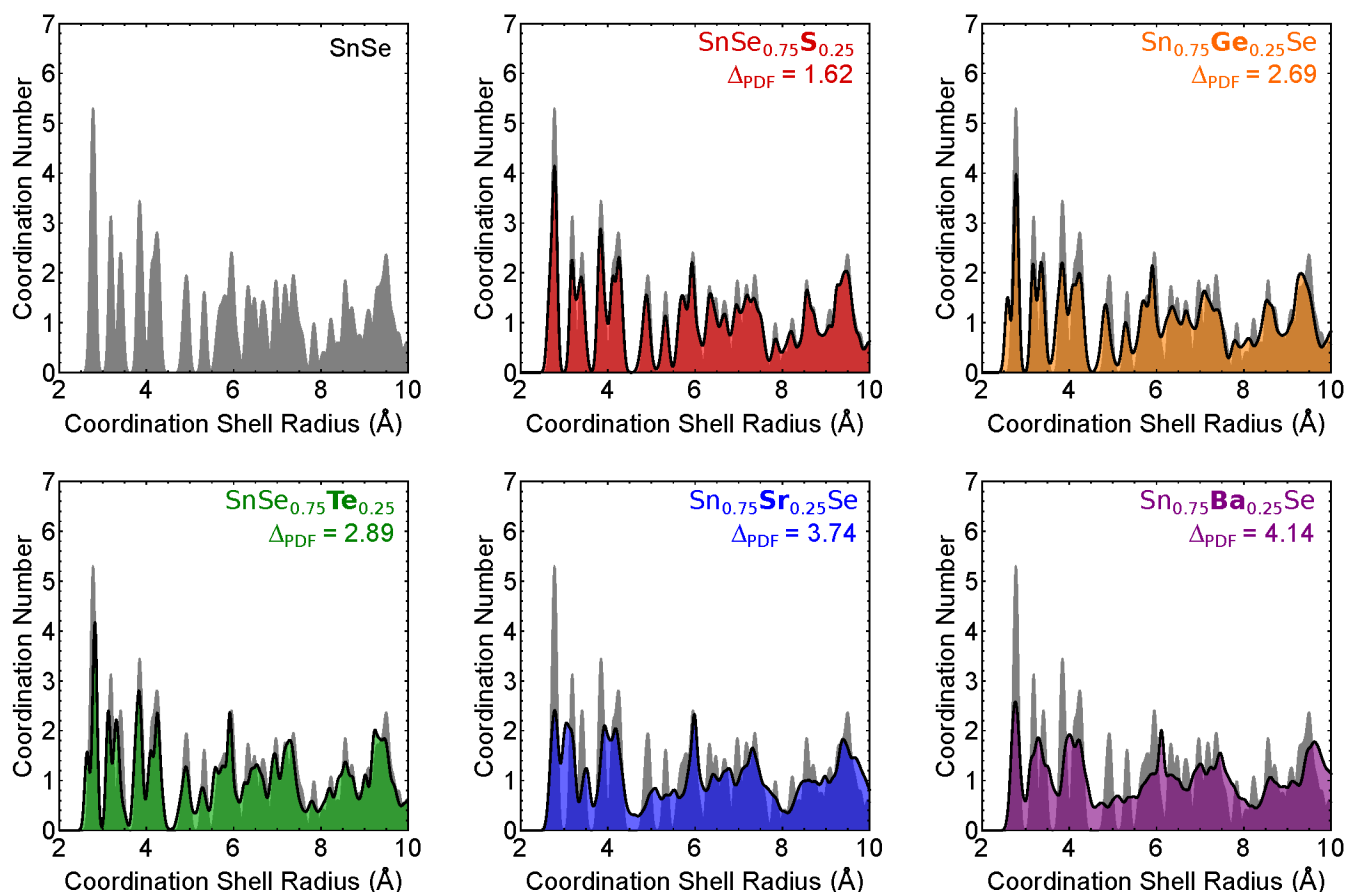
effect of alloying on the coordination environment of SnSe. To ensure the effect is evident, we chose to examine alloy concentrations of 25 mol% while using the special quasi-random structure (SQS) approach to construct supercells. Experimental results do not examine the thermal conductivity at concentrations of 25 mol%, but the results are expected to be predictive provided that defect-defect interactions are not a dominant effect.

Figure 9 presents the PDFs of all five alloys of SnSe at 25 mol%, along with a reference pattern for pure SnSe. Qualitatively, one immediately sees that the peaks associated with pure SnSe are largely preserved for S, Ge, and Te whereas Sr and Ba alloys show significant distortions and a ‘smearing’ of their PDF profiles. To obtain a quantitative measure of the distortion between pure SnSe and the alloyed systems, we construct an integrated difference profile:

$$\Delta_{\text{PDF}} = \int_0^{r_{\text{max}}} |\text{PDF}_{\text{SnSe}}(r) - \text{PDF}_{\text{Alloy}}(r)| dr \quad (19)$$

where  $\text{PDF}_{\text{SnSe}}(r)$  and  $\text{PDF}_{\text{Alloy}}(r)$  are the pair-distribution functions for pure and alloyed SnSe, respectively. The integral bound  $r_{\text{max}}$  is kept relatively small ( $10 \text{ \AA}$ ) to minimize accumulation of computational errors due to finite supercell size. The  $\Delta_{\text{PDF}}$  provides a single scalar which can be used to compare the net change in bonding between the different alloys (Table 3). The PDF approach directly examines change in coordination (bonding) environment of a given structure. As such, it directly probes changes in the bond length (strain) and implicitly carries information regarding loss of atomic registry.

**Computational Summary:** Examination of Table 3 reveals consistent trends for the impact of alloying on the lattice distortion. Considering  $\Delta_{\text{PDF}}$  and  $\Delta_{\text{SAD}}$ , we find that the approaches are internally consistent, with the distortion



**Fig. 9** Changes in the PDF pattern, and the associated distortion metric  $\Delta_{\text{PDF}}$  provide a measure of the distortion in coordination induced by a given alloy (colored) relative to pure SnSe (gray). In systems containing S, Ge, and Te, the change is relatively minimal. The underlying SnSe structure is largely preserved, both in peak position and intensity. However, systems containing Sr and Ba show significantly more distortion. PDF peaks become less defined, smearing and giving rise to additional peaks not seen in the pure SnSe. This is conceptually consistent with the crystallographic changes suggested by the b/c ratio and the correspondingly larger decreases in thermal conductivity in alloys of Ba and Sr.

**Table 3** Summary of numerical results from computation reveals trends between  $B_0$ ,  $\Delta_{\text{PDF}}$ , and  $\Delta_{\text{SAD}}$ . Specifically, as we see increased levels of bond strain, loss of atomic registry, and changes in local coordination (as denoted by increasing values of  $\Delta_{\text{PDF}}$  and  $\Delta_{\text{SAD}}$ , we also observe a softening of the bulk modulus. There is no obvious trend between  $B_0'$  and the other parameters

Alloy	$B_0$ (GPa)	$\Delta_{\text{PDF}}$ (Å)	$\Delta_{\text{SAD}}$ (Å)	$B_0'$
SnSe	42.2	0	0	6.68
S	40.8	1.62	0.38	7.88
Ge	39.9	2.69	0.54	5.35
Te	38.1	2.89	0.92	10.7
Sr	34.3	3.74	1.86	14.4
Ba	31.5	4.14	2.96	9.63

of  $\text{Ba} > \text{Sr} > \text{Te} > \text{Ge} > \text{S}$ . Additionally, the softening of the lattice, as measured by  $B_0$ , follows this same trend. No such obvious trends emerge for  $B_0'$ ; however, this term is a higher order quantification of the bond strength between atoms and may not be expected to trend with total displacement in an anisotropic material. In concert, these results suggest that the Ba alloys should have the strongest scattering, followed by Sr, Te, Ge, and ending with the weakest strain scatterer, S. Results agree well with experimental observations.

### 3.3 Discussion

To provide insight into the design and discovery of materials with strong strain field scattering, we (a) consider the efficacy

of the computationally tractable descriptors developed herein to predict  $\Gamma_s'$ , (b) assess the broader implications concerning strain field chemistry that emerge from the SnSe model system and (c) highlight opportunities and remaining challenges poised by point-defect induced strain fields.

*Computational Assessment of  $\Gamma_s'$*  We note that the relative ranking of the alloys in terms of increasing  $\Delta_{\text{PDF}}$ , increasing  $\Delta_{\text{SAD}}$ , and decreasing  $B_0$  is consistent with experimental observations. This is to say, all three computational approaches and the experimental data lead to the same conclusion:  $\kappa_{\text{Ba}} < \kappa_{\text{Sr}} < \kappa_{\text{Te}} < \kappa_{\text{Ge}} < \kappa_{\text{S}}$ . While the approaches appear consistent with each other, it is worth considering *why* the relatively simply computational approaches are predictive of the experimentally observed strain scattering  $\Gamma_s'$ .

To assess the relative merit of potential point defect candidates in reducing the lattice thermal conductivity, we generally require two pieces of knowledge: mass scattering and strain scattering. While mass contrast is a relatively trivial parameter to compute, strain scattering is significantly less predictable. Even if the atomic radii are well-established, the magnitude of  $\varepsilon$  is not known *a priori*. To this end, we proposed the use of  $\Delta_{\text{SAD}}$ ,  $B_0$ , and  $\Delta_{\text{PDF}}$  as computationally efficient methods of probing the nature of  $\Gamma_s'$  in isoelectronic alloys. Figure 10 compares the  $\Gamma_s'$  values obtained from experimental measurements of the five SnSe alloys against  $\Delta_{\text{SAD}}$ ,  $B_0$ , and  $\Delta_{\text{PDF}}$ .

Figure 10a considers the SAD approach to predict strain-field based phonon scattering. The associated parameter  $\Delta_{\text{SAD}}$  principally examines the change in atomic positions under the

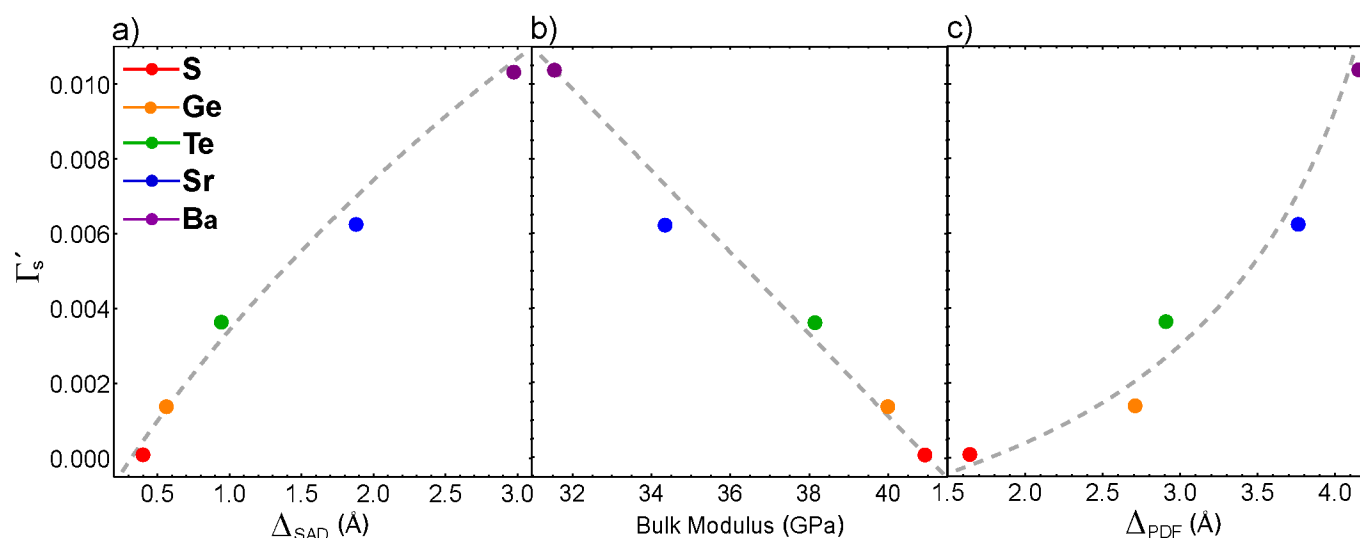


**Fig. 10** Plots demonstrating relationship between experimentally calculated  $\Gamma_s'$  and computationally calculated  $\Delta_{\text{PDF}}$ , bulk modulus, and  $\Delta_{\text{SAD}}$ . Although visually identical curves are obtained for all other experimental compositions, only  $\Gamma_s'$  corresponding to 1 mol% data is shown for clarity. Grey dashed lines are intended as guides to the eye, and are not meant to convey any mathematical significance. We note strong trends in all data sets, implying that the  $\Delta_{\text{PDF}}$ , the bulk modulus, and  $\Delta_{\text{SAD}}$  are relevant metrics for the prediction of the experimentally realizable strain scattering in SnSe.

influence of an impurity atom. In essence,  $\Delta_{\text{SAD}}$  examines the change in spatial registry of atomic nuclei. However, changes in atomic positions also imply changes in bond length and bond strain. Thus,  $\Delta_{\text{SAD}}$  also implicitly contains information about bond strain. We see a strong positive trend between  $\Delta_{\text{SAD}}$  and  $\Gamma'_s$ , suggesting that the SAD is well-correlated with the experimentally observed strain scattering. Sulfur alloying leads to minimal shifts of atomic position (Figure 8) and likewise has a null value for  $\Gamma'_s$ . In contrast, Ba exhibits major strain distortions and leads to a large  $\Gamma'_s$  when the experimental data is fit.

Figure 10b demonstrates the correlation between the computed bulk modulus  $B_0$  and  $\Gamma'_s$ . Recall that  $B_0$  provides an average measure of the harmonic force constants between bonds. As the computed value decreases, it implies a strong softening of bonds in the vicinity of the point defect. In essence,  $B_0$  examines the change in the registry of bond force constants. As with  $\Delta_{\text{SAD}}$ , a strong trend is observed. It should be noted that the changes in  $B_0$  are quite large given the alloy level is 25 mol%.

While bulk modulus only provides information regarding harmonic behavior, the pressure derivative of the bulk modulus  $B'_0$  provides an estimate of anharmonicity. Here,  $B'_0$  is obtained from analyzing the calculated structures using the Murnaghan equation of state and associated formalism. \* Inspection of  $B'_0$  in Table 3 generally suggests the most distorted lattices exhibit the largest changes in  $B'_0$ ; however no clear trend with  $\Gamma'_s$  emerges. This suggests that anharmonicity changes are not the dominant trend controlling point defect scattering in SnSe. Nevertheless, it is interesting to observe that significant changes in  $B'_0$  occur in some alloys. These calculations suggest that there is the potential to additionally control anharmonicity via alloying. Such alloys may not require large mass contrast or strain fields, as their utility would be focused on increasing Umklapp scattering.

Finally, Figure 10c shows there is a strong positive correlation between the PDF analysis and  $\Gamma'_s$ . Even though both  $\Delta_{\text{PDF}}$  and  $\Delta_{\text{SAD}}$  approaches appear to capture the underlying strain field well, it is worth examining the differences in these two approaches. Recall that  $\Delta_{\text{PDF}}$  is obtained from a high concentration alloy using a SQS supercell and directly considers the inter-atomic strain induced by the defects. In contrast,  $\Delta_{\text{SAD}}$  considers a single defect and directly maps the loss of crystalline registry of individual atoms. Other than the differences in concentrations employed (and associated defect-defect interactions), these differences are fairly subtle as loss of registry leads to bond strains and vice versa.

#### *Implications and Challenges for Strain Field Design:*

\* While  $B'_0$  is not equivalent to the Grüneisen parameter, the response of the bulk modulus to an isothermal compression may provide a description of the underlying anharmonicity of the force constants.

Commonly applied models for the investigation of alloy scattering (e.g. Abeles) often abstract the concept of strain-based scattering into a parameter with little physical insight ( $\epsilon$ ). While this approach is acceptable for analysis of experimental data, it doesn't provide the insight required to predict the effect of various alloying species on thermal conductivity *ab initio*. This work has provided new parameters, accessible through computation, which can guide experimental work towards effective alloys.

As we've demonstrated in SnSe, the distortion (strain) fields which are induced by a isolated defect are extended in nature and have profound effects on the thermal conductivity. For example, in the case of an isolated Ba atom (SAD approach), the strain field extends across a 1 nm diameter. Furthermore, the individual atomic displacements are large (approaching 0.5 Å) and the effect on the inter-atomic forces (as considered via bulk modulus) is significant. Overall, we demonstrate that the influence of an atomic substitution is much more nuanced and involved than would be anticipated by the classical description of a 'point defect.'

The increased complexity might suggest that the computational assessment of the effect of point defect scattering on the lattice thermal conductivity should be challenging. However, we have demonstrated that the computationally simple metrics  $\Delta_{\text{SAD}}$ ,  $\Delta_{\text{PDF}}$ , and  $B_0$  correlate well with the experimentally observed strain scattering in SnSe. This is to say, we do not need to explicitly consider the nuances of structural changes in the vicinity of the point defects to have computationally accessible methods of predicting the efficacy of a point defect on thermal conductivity depression. This opportunity arises from the broad range of phonons present in a material, each of which is going to interact differently with a strain field. It is also interesting to note that consideration of unit cell volume alone is not predictive of the scattering strength; for example the significant contraction in unit cell volume experienced by S or Ge alloys does not lead to strong strain field scattering.

Tuning of thermal conductivity by point defect scattering carries some inherent advantages over nanostructuring, which has been thoroughly investigated over the last two decades.<sup>14–20</sup> At the dilute limit, the local strain fields should be identical around each defect. Thus, the ability to engineer particular types of strain fields is far more controlled than nanostructuring. Point defects are also attractive due to their thermodynamic stability. Unlike nanostructuring which is subject to grain growth and Ostwald Ripening, solubility of a particular defect generally increases with increasing temperature, lending further stability to the defect. Additionally, by not disrupting the overall crystallinity, anisotropic materials can be developed that harness particularly attractive transport along specific crystallographic directions.

However, lowering the thermal conductivity via point defect scattering is not without challenges. For example, the induced

strain fields and corresponding changes in atomic periodicity may also effect the electronic components of  $zT$ . This requires the identification of point defects whose effect on electronic transport is either benign or outweighed by the effect on the thermal conductivity. Additionally, the degree of point defect integration ultimately depends on the thermodynamic solubility of the constituent species. The largest strain fields are often induced by species with low solubility, placing an additional constraint on the degree to which point defects can be utilized. In the case of Ba and Sr alloys of SnSe, it may be that the energetic proximity to the  $Cmcm$  phase creates an opportunity to access higher solubilities than might be expected for such large strain fields.

### 3.4 Conclusion

Historically, the point defect scattering strength has followed from simple considerations such as mass contrast and the presence of induced strain fields. However, the exact nature of the strain fields is rarely studied in detail. This work combined experimental measurements and computational models to create three simple, efficient computational metrics for parameterizing the strain component of point defect scattering: (i) the single-atom distortion model (SAD) and associated  $\Delta_{\text{SAD}}$  to assess the change in atomic registry under the influence of a single alloying atom, (ii) the bulk modulus  $B_0$  to consider the change in average, harmonic bond force constants in the alloyed species, and (iii) the pair-distribution function (PDF) and associated  $\Delta_{\text{PDF}}$  to quantify the changes in bond strain between alloyed and pure SnSe. We verify our methods using the model system, SnSe, and associated alloys of S, Te, Ge, Sr, and Ba. Our work demonstrates that the strength and extent of the induced strain fields depend heavily on defect chemistry. Results are consistent with the classical models, but our computational methods also provide insight into the underlying scattering physics (i.e. registry loss, bond strain, anharmonicity, etc), which would normally be attributed to the poorly defined concepts of  $\epsilon$  and the atomic radii. In doing so, we provide a means to screen alloys and engineer materials using point defects. The methods presented here are conceptually transparent, computationally inexpensive, and chemically versatile enough to additionally enable the high throughput evaluation of point defect scattering. This work suggests that the underlying physics of point defect scattering is richer than classical models would suggest. By augmenting existing high throughput searches with the techniques contained herein, point defect scattering can become a core facet of materials design and thermoelectric material optimization.

## 4 Acknowledgements

This work was supported by the US Department of Energy under contract No. DE-AC36-08GO28308 to NREL, within the Laboratory Directed Research and Development program. The use of high performance computing resources of NREL's Computational Science Center is gratefully acknowledged. E.S.T., B.R.O., and A.L. acknowledge support from the National Science Foundation under Grant 1334713. The authors thank Prashun Gorai, Lauryn Baranowski, and Vladan Stevanović for their valuable discussions.

## References

- 1 G. J. Snyder and E. S. Toberer, *Nature Mater.*, 2008, **7**, 105–114.
- 2 L. Baranowski, G. J. Snyder and E. S. Toberer, *Energy Environ. Sci.*, 2012, **5**, 9055.
- 3 L. Bell, *Science*.
- 4 C. Wood, *Rep. Prog. Phys.*, 1988, **51**, 459–539.
- 5 E. S. Toberer, A. Zevkink and G. J. Snyder, *J. Mater. Chem.*, 2011, **21**, 15843–15852.
- 6 S. Wang, Z. Wang, W. Setyawan, N. Mingo and S. Curtarolo, *Phys. Rev. X*, 2011, **1**, 021012.
- 7 J. Carrete, W. Li, N. Mingo, S. Wang and S. Curtarolo, *Phys. Rev. X*, 2014, **4**, 011019.
- 8 G. K. H. Madsen, *J. Am. Chem. Soc.*, 2006, **128**, 12140.
- 9 J. Yang, H. Li, T. Wu, W. Zhang, L. Chen and J. Yang, *Adv. Funct. Mater.*, 2008, **18**, 2880.
- 10 J. Yan, P. Gorai, B. Ortiz, S. Miller, S. Barnett, T. Mason, V. Stevanović and E. S. Toberer, *Energy Environ. Sci.*, 2015, DOI: 10.1039/C4EE03157A.
- 11 C. B. Vining, W. Laskow, J. O. Hanson, R. R. van der Beck and P. D. Gorsuch, *J. Appl. Phys.*, 1991, **69**, 4333–4340.
- 12 C. B. Vining, *J. Appl. Phys.*, 1990, **69**, 331–341.
- 13 Y. Pei, X. Shi, A. LaLonde, H. Wang, L. Chen and G. J. Snyder, *Nature*, 2011, **473**, 66–69.
- 14 C. J. Vineis, A. Shakouri, A. Majumdar and M. G. Kanatzidis, *Adv. Mater.*, 2010, **22**, 3970–3980.
- 15 A. J. Minnich, M. S. Dresselhaus, Z. F. Ren and G. Chen, *Energy Environ. Sci.*, 2009, **2**, 466–479.
- 16 C. J. Vineis, A. Shakouri, A. Majumdar and M. G. Kanatzidis, *Adv. Mater.*, 2010, **22**, 3970–3980.
- 17 S. K. Bux, J. P. Fleurial and R. B. Kaner, *Chem. Commun.*, 2010, **46**, 8311–8324.
- 18 A. J. Minnich, M. S. Dresselhaus, Z. F. Ren and G. Chen, *Energy Environ. Sci.*, 2009, **2**, 466–479.
- 19 S. K. Bux, R. G. Blair, P. K. Gogna, H. Lee, G. Chen, M. S. Dresselhaus, R. B. Kaner and J. P. Fleurial, *Adv. Funct. Mater.*, 2009, **19**, 2445–2452.
- 20 Y. Pei, J. Lensch-Falk, E. S. Toberer, D. L. Medlin and G. J. Snyder, *Adv. Funct. Mater.*, 2011, **21**, 241–249.
- 21 G. P. Meisner, D. T. Morelli, S. Hu, J. Yang and C. Uher, *Phys. Rev. Lett.*, 1998, **80**, 3551–3554.
- 22 M. Zebarjadi, K. Esfarjani, J. Yang, Z. F. Ren and G. Chen, *Phys. Rev. B*, 2010, **83**, 195207.
- 23 J. Yang, D. T. Morelli, G. P. Meisner, W. Chen, J. S. Dyck, and C. Uher, *Phys. Rev. B*, 2003, **67**, 165207.
- 24 M. M. Koza, M. R. Johnson and H. Mutka, *Phys. Rev. B*, 2010, **82**, 214301.
- 25 Y. Takasu, T. Hasegawa, N. Ogita, M. Udagawa, M. A. Avila, K. Suekuni, and T. Takabatake, *Phys. Rev. B*, 2010, **82**, 134302.

- 26 R. P. Hermann, W. Schweika, O. Leupold, R. Rüffer, G. S. Nolas, F. Grandjean and G. J. Long, *Phys. Rev. B*, 2005, **72**, 174301.
- 27 E. S. Toberer, A. F. May and G. J. Snyder, *Chem. Mater.*, 2010, **22**, 624–634.
- 28 C. B. Vining, W. Laskow, J. O. Hanson, R. R. V. der Beck and P. D. Gorsuch, *J. of Appl. Phys.*, 1991, **69**.
- 29 A. May, E. Flage-Larsen and G. Snyder, *Phys. Rev. B*, 2010, **81**, 125205.
- 30 B. Abeles, *Phys. Rev.*, 1963, **131**, 1906–1911.
- 31 W. Li, L. Lindsay, D. A. Broido, D. A. Stewart and N. Mingo, *Phys. Rev. B*, 2012, **86**, 174307.
- 32 L. Lindsay, D. A. Broido and T. L. Reinecke, *Phys. Rev. Lett.*, 2012, **109**, 095901.
- 33 T. Chattopadhyay, J. Pannetier and H. G. von Schnering, *J. Phys. Chem. Solids*, 1986, **47**, 879–885.
- 34 H. Wiedemeier and H. G. von Schnering, *Z. Kristallogr.*, 1978, **148**, 295–303.
- 35 D. I. Bletskan, V. S. Gerasimenko, and V. V. Khimnets, *Russ. J. Inorg. Chem.*, 1981, **26**, 409–411.
- 36 M. I. Karakhanova, M. E. Tamm, and A. V. Novoselova, *Inorg. Mater.*, 1976, **12**, 793–795.
- 37 L. Zhao, S. Lo, Y. Zhang, H. Sun, G. Tan, C. Uher, C. Wolverton, V. P. Drabid and M. G. Kanatzidis, *Nature*, 2014, **508**, 373–377.
- 38 C. Chen, H. Wang, Y. Chen, T. Day and G. J. Snyder, *J. Mater. Chem. A*, 2014, **2**, 11171.
- 39 A. C. Larson and R. B. V. Dreele, *Los Alamos National Laboratory Repory LAUR 86-748*, 1994.
- 40 B. H. Toby, *J. Appl. Cryst.*, 2001, **34**, 210–213.
- 41 D. A. G. Bruggeman, *Ann. Phys.*, 1935, **24**, 636–664.
- 42 D. A. G. Bruggeman, *Ann. Phys.*, 1936, **25**, 645–671.
- 43 A. Zunger, S. Wei, L. Ferreira and J. Bernard, *Phys. Rev. Lett.*, 1990, **65**, 353–356.
- 44 A. van de Walle, P. Tiwary, M. de Jong, D. Olmsted, M. Asta, A. Dick, D. Shin, Y. Wang, L. Q. Chen, and Z. K. Liu, *Calphad*, 2013, **42**, 13–18.
- 45 G. Kresse and D. Joubert, *Phys. Rev. B*, 1999, **59**, 1758–1775.
- 46 J. P. Perdew and A. Zunger, *Phys. Rev. B*, 1981, **23**, 5048–5078.
- 47 P. E. Blöchl, *Phys. Rev. B*, 1994, **50**, 17953–17979.
- 48 J. P. Perdew, K. Burke, and M. Erzerhof, *Phys. Rev. Lett.*, 1996, **77**, 3865–3868.
- 49 F. Murnaghan, *Proc. Natl. Acad. Sci. USA*, 1944, **30**, 244.
- 50 V. Leute and D. Menge, *Z. Phys. Chem.*, 1992, **176**, 47–64.
- 51 E. A. Galiulin, I. N. Odin and A. V. Novoselova, *Russ. J. Inorg. Chem.*, 1982, **27**, 152–153.
- 52 J. Callaway, *Phys. Rev.*, 1959, **113**, 1044–1051.
- 53 M. G. Holland, *Phys. Rev.*, 1963, **132**, 2461–2471.
- 54 M. Roufosse and P. G. Klemens, *Phys. Rev. B*, 1973, **7**, 5379–5386.
- 55 J. E. Parrott, *J. Phys. C*, 1969, **2**, 147–151.
- 56 H. J. Goldsmit and A. W. Penn, *Phys. Lett.*, 1968, **27A**, 523–524.
- 57 J. D. Chung, A. J. H. McGaughey and M. Kaviani, *J. Heat Trans.*, 2004, **126**, 691–696.
- 58 P. G. Klemens, *Proc. Phys. Soc.*, 1955, **68**, 1113–1128.
- 59 Z. Zhou, C. Uher, A. Jewell and T. Caillat, *Phys. Rev. B*, 2005, **71**, 235209.
- 60 J. Yang, G. P. Meisner and L. Chen, *Appl. Phys. Lett.*, 2004, **85**, 1140–1142.
- 61 M. Zhou, L. Chen, W. Zhang and C. Feng, *J. Appl. Phys.*, 2005, **98**, 013708.
- 62 E. S. Toberer, L. L. Baranowski and C. Dames, *Annu. Rev. Mater. Res.*, 2012, **42**, 179–209.

## 5 Supplementary

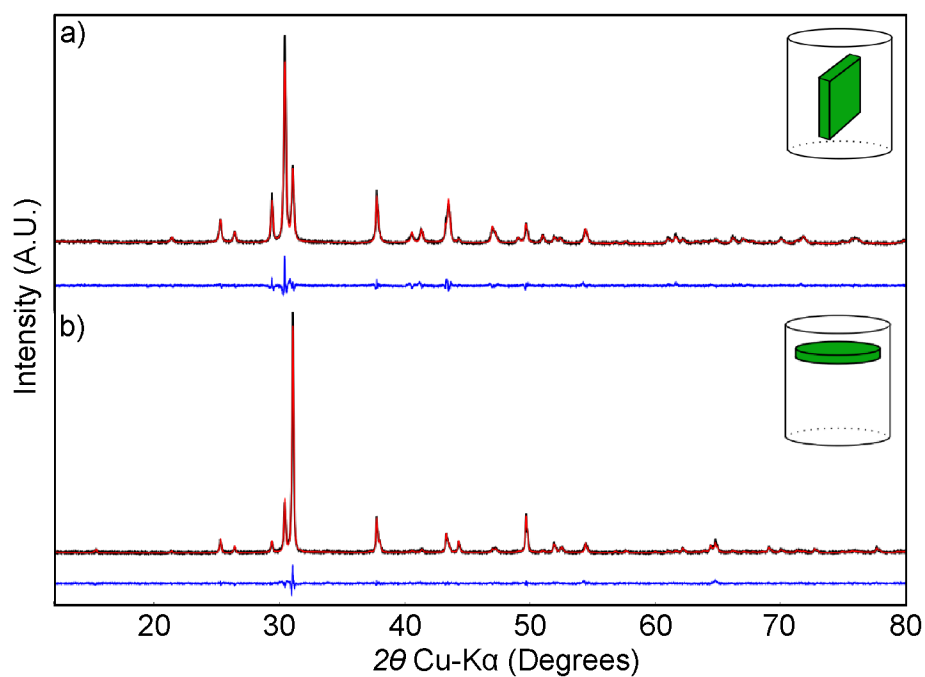


**Fig. S1** XRD scans of pure, polycrystalline SnSe cut along different directions. a) Samples cut with primary face perpendicular to press direction are consistent with randomly textured polycrystalline SnSe. Rietveld fits (red) match experimental (black) data exceptionally well, confirming that the material is phase pure and of good crystalline quality. b) Samples cut with the primary face perpendicular to the press axis exhibit strong texturing in the (040) direction. Transport is expected to be anisotropic in SnSe, so textured samples are an additional complication we opted to avoid.

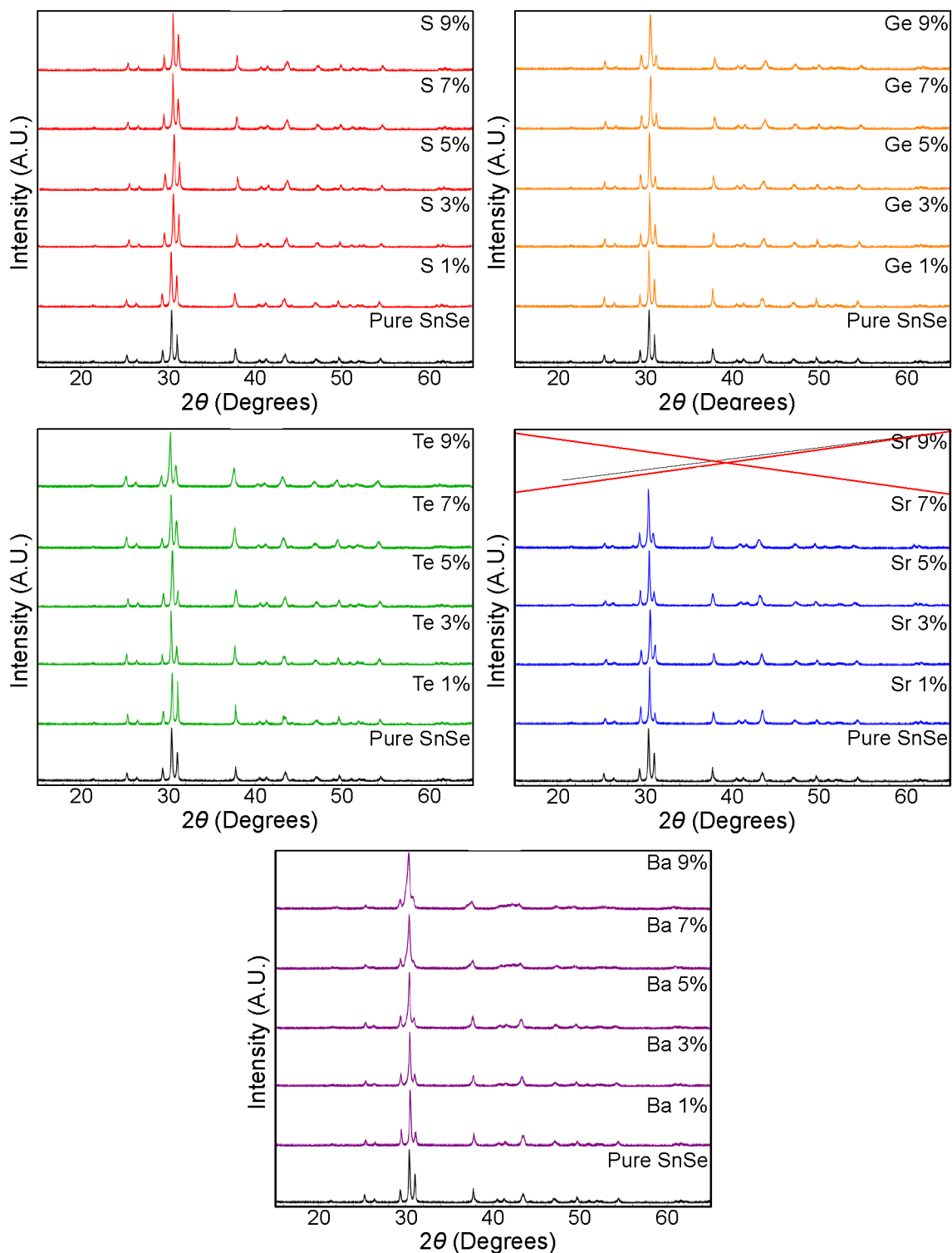


**Fig. S2** All XRD patterns collected for alloyed plates of SnSe. Note that the 9 mol% Sr sample was not collected because phase separation was already observed at 7 mol%. Texturing is not completely consistent between all samples, but the degree of variation is relatively small with the exception of the 1 mol% Te sample. This is consistent with the discrepancy observed in Figure 7 for the 1 mol% Te sample.

**Table S1** Experimental speed of sound measurements performed on 5 mol% alloys of SnSe show no obvious trends. Errors shown represent  $3\sigma$  from the mean value. Relatively large experimental error prohibits the significant conclusions from being drawn, particularly with regards to the effect of alloying species on the speed of sound.

Alloy	$v_{shear}$ (m/s)	$v_{long}$ (m/s)	$v_{sound}$ (m/s)
SnSe	$1330 \pm 90$	$2020 \pm 170$	$1560 \pm 210$
SnSe <sub>0.95</sub> S <sub>0.05</sub>	$1250 \pm 49$	$1890 \pm 180$	$1460 \pm 190$
Sn <sub>0.95</sub> Ge <sub>0.05</sub> Se	$1290 \pm 50$	$1980 \pm 140$	$1520 \pm 160$
SnSe <sub>0.95</sub> Te <sub>0.05</sub>	$1440 \pm 75$	$2290 \pm 140$	$1730 \pm 180$
Sn <sub>0.95</sub> Sr <sub>0.05</sub> Se	$1420 \pm 22$	$2280 \pm 66$	$1710 \pm 73$
Sn <sub>0.95</sub> Ba <sub>0.05</sub> Se	$1300 \pm 21$	$2030 \pm 67$	$1550 \pm 74$

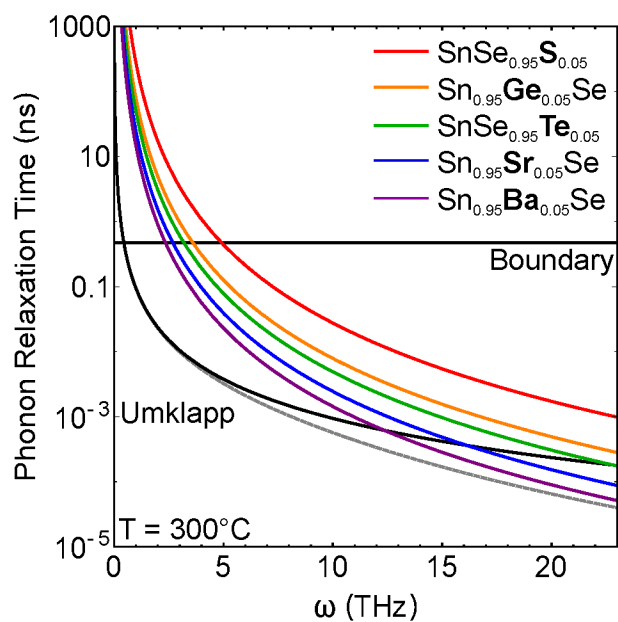


**Fig. S3** Curves illustrating the functional dependence of the phonon scattering terms  $\tau_U$ ,  $\tau_B$ , and  $\tau_{PD}$  on alloy species for 5 mol% samples. Umklapp and boundary scattering are fixed at values refined from pure SnSe. Notably, Umklapp scattering is the dominant scattering phenomenon in all systems except those containing Ba and Sr, in which point-defect scattering begins to dominate midway through the acoustic phonon frequencies. Boundary scattering contributes only weakly to the net relaxation time, generally dominated by Umklapp scattering except at very low phonon frequencies.

**Table S2** Summary of some parameters of interest for all alloys after refinement with the Abeles model. Shown are  $\varepsilon$ ,  $\Gamma_m$ , and  $\Gamma_s$  from the classical Abeles approach, the ratio of strain to mass scattering, and  $\Gamma'_s$ . Note that  $\varepsilon$  is composition *independent*, although all other parameters are explicitly dependent on composition by definition. The numerical value of  $\varepsilon$  is provided for transparency, although it is extremely sensitive to choice of radii and is not a numerically robust quantity. We note that the total and strain field scattering parameters track well with computational predictions.

Alloy	$\varepsilon$	$\Gamma_m$	$\Gamma_s$	$\Gamma_{tot}$	$\Gamma_s/\Gamma_m$	$\Gamma'_s$
S(1mol%)	0	0.0011	0	0.0011	0	0
S(3mol%)	0	0.0033	0	0.0033	0	0
S(5mol%)	0	0.0055	0	0.0055	0	0
S(7mol%)	0	0.0076	0	0.0076	0	0
S(9mol%)	0	0.0010	0	0.0010	0	0
Ge(1mol%)	14	0.0011	0.0019	0.0030	1.73	0.0013
Ge(3mol%)	14	0.0032	0.0055	0.0087	1.70	0.0038
Ge(5mol%)	14	0.0053	0.0089	0.0142	1.69	0.0063
Ge(7mol%)	14	0.0073	0.0122	0.0195	1.67	0.0087
Ge(9mol%)	14	0.0093	0.0154	0.0247	1.65	0.0110
Te(1mol%)	32	0.0012	0.0023	0.0035	1.92	0.0036
Te(3mol%)	32	0.0035	0.0068	0.0103	1.95	0.0104
Te(5mol%)	32	0.0056	0.0112	0.0168	1.99	0.0168
Te(7mol%)	32	0.0076	0.0154	0.0230	2.02	0.0230
Te(9mol%)	32	0.0095	0.0195	0.0290	2.06	0.0287
Sr(1mol%)	490	0.0005	0.0089	0.0094	18.0	0.0062
Sr(3mol%)	490	0.0015	0.0260	0.0275	17.9	0.0181
Sr(5mol%)	490	0.0024	0.0423	0.0447	17.8	0.0297
Sr(7mol%)	490	0.0033	0.0579	0.0612	17.6	0.0407
Sr(9mol%)	490	0.0042	0.0727	0.0769	17.5	0.0514
Ba(1mol%)	402	0.0002	0.0148	0.0441	84.4	0.0102
Ba(3mol%)	402	0.0005	0.0436	0.0275	84.7	0.0301
Ba(5mol%)	402	0.0008	0.0712	0.0720	85.0	0.0491
Ba(7mol%)	402	0.0011	0.0976	0.0987	85.3	0.0670
Ba(9mol%)	402	0.0014	0.1227	0.1241	85.6	0.0841

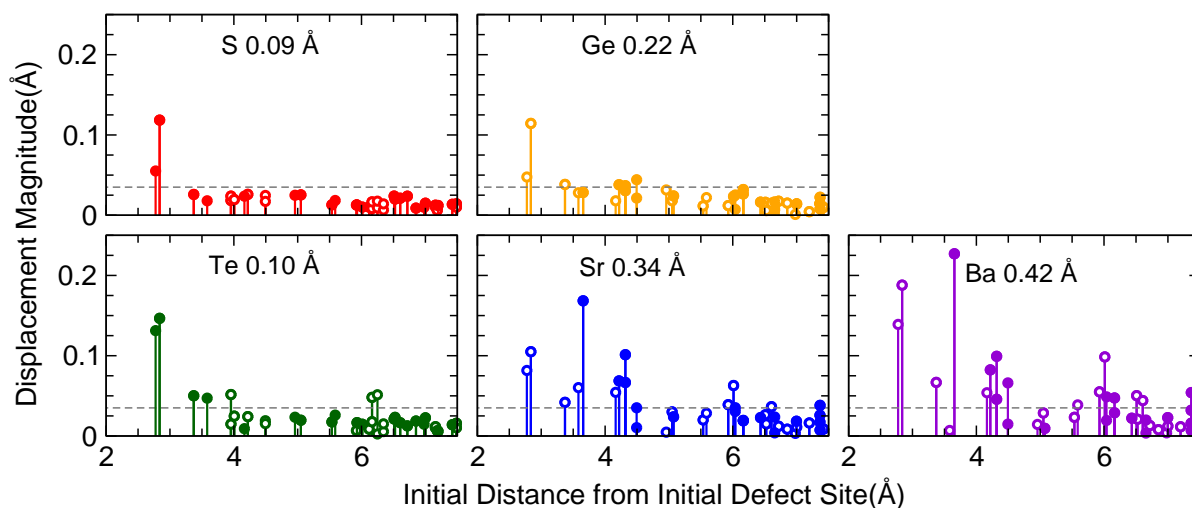


**Fig. S4** Distribution of the magnitude of individual atomic displacements from the Single Atom Distortion computational model. Filled circles denote Sn atoms, empty circles denote Se. The thermal cutoff, marked by the dashed gray line, indicates the threshold where computational error can no longer be distinguished from meaningful displacement data. This is most evident in the sulfur sample. We expect that the distortions near the sulfur defect should decay quickly as a function of distance from the defect, as SnS shares the same crystal structure as SnSe. Computationally, we observe several moderate distortions before the values plateau further from the defect site. We define the thermal cutoff slightly above the plateau, which is approximately 0.4 Å. Similar behavior is observed for Ge and Te. Sr and Ba demonstrate stronger, more widely distributed defects, but are expected to plateau if a larger supercell is used.